The 8th International Supercritical CO_2 Power Cycles Symposium
February 27 – 29, 2024, San Antonio, Texas
Paper #27

Study on the initial position of Taylor vortex for Taylor-Couette-Poiseuille flow formed by supercritical carbon dioxide

Fengxiong Lu
PhD candidate
IET
UCAS
Beijing, China

Chaohong Guo
Associate Researcher
IET
UCAS
Beijing, China

Shijie Zhang
Researcher
IET
UCAS
Beijing, China

Buze Chen
Master degree candidate
IET
UCAS
Beijing, China

Bo Wang
Associate Researcher
IET
UCAS
Beijing, China

Xiang Xu
Researcher
IET
UCAS
Beijing, China

Fengxiong Lu: A current doctoral candidate at the University of Chinese Academy of Sciences, primarily focuses on researching the flow and heat transfer characteristics of supercritical carbon dioxide within a rotating turbine disk.

Chaohong Guo: An associate researcher with the Institute of Engineering Thermophysics at the Chinese Academy of Sciences, focuses on investigating the heat transfer principles of supercritical carbon dioxide in rotating flow and the aerodynamic theory of supercritical carbon dioxide expanders.

Shijie Zhang: A researcher at the Institute of Engineering Thermophysics, Chinese Academy of Sciences, focuses on analyzing heavy-duty gas turbine performance and comprehensive design research, advanced optimization of gas turbine cycles, and research into the optimization and integration of distributed energy supply systems.
Buze Chen：Currently studying for a master degree at the University of Chinese Academy of Sciences. The main research direction is turbine wind friction losses.
Bo Wang: Associate researcher at the Institute of Engineering Thermophysics, Chinese Academy of Sciences. The main research direction is the dynamic simulation and control of supercritical carbon dioxide power generation systems and new energy power systems.
Xiang Xu：A researcher at the Institute of Engineering Thermophysics, Chinese Academy of Sciences. The main research directions are advanced energy power system research and clean and efficient conversion of carbon-containing energy.
Corresponding Author: Chaohong Guo. email: guochaohong@iet.cn.

ABSTRACT

Supercritical carbon dioxide creates a typical Taylor-Couette-Poiseuille flow within the annular gap of a rotating turbomachinery. The spatial variation characteristic of Taylor vortices generated in this flow is crucial for maintaining the stability of the rotating turbomachinery. In order to predict the spatial variation laws of the Taylor vortex formed by the supercritical carbon dioxide working fluid in the rotating annular gap, this paper combines the actual work process of the supercritical carbon dioxide turbine shaft, using Fluent and Matlab tools, investigating the variation law of Taylor

vortex within the rotation speed range 0~50000RPM. The results demonstrated that the formation of Taylor vortices in this range is significantly influenced by the aspect ratio and radius ratio of the annular gap, the axial Reynolds number and the Taylor number of the flow. The stability of the rotating flow can be enhanced by reducing the aspect ratio, increasing the radius ratio, increasing the axial Reynolds number, and decreasing the Taylor number, thereby suppressing the formation of Taylor vortices. Finally, in our study, multivariate matrix exponential regression model and a neural network algorithm in Matlab have been established to capture the intricate interplay between the initial position of the Taylor vortex and critical parameters, namely the aspect ratio, radius ratio, axial Reynolds number, and Taylor number.

INTRODUCTION

The supercritical carbon dioxide(sCO_2) Brayton cycle stands as a crucial technology in the realm of future energy transformation and carbon reduction. This significance owes itself to its remarkable efficiency, compact engineering, cost-effective operation, and robust environmental credentials[1, 2]. At one of the heart of this cycle lies the sCO_2 turbine[3], which typically operates at around 500°C[4, 5]. Ensuring its reliable performance hinges on the prevalent method of employing dry gas sealing technology, renowned for its minimal gas leakage and outstanding sealing properties[6, 7]. The typical operating temperature range for dry gas seals does not usually exceed 200°C[7]. Due to the close proximity between the inlet of the sCO_2 turbine and the dry gas seal, it is essential to cool the turbine rotor within a confined space. This poses a significant challenge in the thermal design of the sCO_2 turbine rotor[7]. The commonly adopted procedure entails the direct utilization of low-temperature supercritical carbon dioxide to cool the rotating shaft [8-11]. As illustrated in Figure 1, sCO_2 demonstrates a characteristic Taylor-Couette-Poiseuille(T-C-P) flow within the gap between the rotating shaft and the stationary casing[11]. T-C-P flow gives rise to evolving Taylor vortices transiently within the rotating annular gap[12]. These Taylor vortices induce fluctuations in pressure and velocity[13], leading to the turbine shaft experiencing impacts and vibrations. Additionally, this phenomenon results in increased power loss during the flow process, ultimately diminishing the mechanical efficiency of the sCO_2 turbine[14]. Therefore, a comprehensive investigation into the formation conditions and evolving patterns of Taylor vortices within the T-C-P flow of sCO_2 within the turbine shaft is crucial for enhancing the performance of sCO_2 turbines.

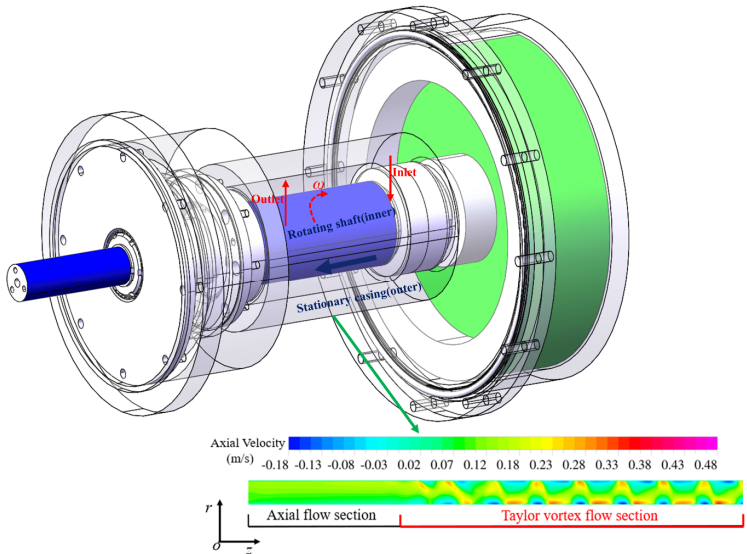

Figure 1. Schematic diagram of sCO_2 turbine shaft.

T-C-P flow is formed by combining axial Poiseuille flow with the basis of Taylor-Couette(T-C) flow. In 1923, Taylor[12]conducted his initial experiment on the flow behavior of a viscous fluid within a coaxially rotating cylinder. His investigation revealed that with an increase in the rotational speed of the inner cylinder, the fluid within the gap manifested a sequence of distinct flow patterns, including the development of Taylor vortices, wavy Taylor vortices, and the modulation of various states involving wavy Taylor vortices and spiral turbulent Taylor vortices[15]. Kaye and Elgar et al.[16] conducted experimental research to investigate the critical Taylor number responsible for inducing Taylor vortices in T-C flow. Marcus et al.[17] investigated the propagation speed of a traveling wave at the critical Reynolds number, transitioning from Taylor vortices to corrugated Taylor vortices. Compared to T-C flow, the introduction of axial flow in T-C-P flow enhances the stability of the viscous fluid within the rotating annular gap, thereby diminishing the probability of Taylor vortices formation[18]·[19]. Werely et al.[20] performed a thorough and insightful investigation into the flow characteristics of T-C flow under axial flow conditions using experimental methods. Following this, Hwang et al. [21] built upon their work with numerical simulations to analyze further and summarize the distinct flow patterns. The radius ratio significantly influences the flow characteristics within the T-C-P flow [22]. Based on Yuki et al. [23] research findings, a high radius ratio yields eight distinct flow states in the T-C-P flow. The vortex structure at a Reynolds number of 10000 can be accurately described by the unsteady Reynolds-averaged Navier-Stokes k-omega Shear-Stress Transport model [24]. Working fluids in these studies include air, water, and other working medium with constant physical properties. However, owing to the dramatic alterations in the physical characteristics of sCO_2 as working fluid (as depicted in Figure 2, which illustrates the profile in the physical properties of sCO_2 in temperatures under 10MPa conditions, with data sourced from REFPROP), coupled with the megawatt sCO_2 turbine shaft speed can reach more than 30000 RPM, this leads to an escalation of the Ta for sCO_2 T-C-P flow up to 10^{11}, and Re_a reaching 10^6, a range that vastly surpasses what is encountered when using media like air and water. Thus far, only the studies conducted by Qin et al. [25], Swann et al. [10, 11, 26], and Chen et al. [7] have focused on examining the heat transfer characteristics of sCO_2 T-C-P flow. Qin et al. [25] conducted a numerical simulation study focusing on the flow of sCO_2 in the annular gap of the bearing. Swann et al. integrated the heat exchange conditions involving the coupling of fluids and solids within the sCO_2 turbine main shafts. They established a test platform for the sCO_2 T-C-P flow and conducted the associated experimental investigations[10, 11, 26]. In addressing the cooling challenge associated with the main shaft of a sCO_2 turbine, Chen et al. [7] and colleagues conducted a study that examined the heat transfer characteristics of sCO_2 within a high-speed rotating annular gap. This investigation considered factors such as aspect ratio, radius ratio, axial Reynolds number, and Taylor number, yielding insightful results. Consequently, they derived an empirical relationship to describe the heat transfer phenomenon. These studies exclusively concentrated on examining the heat transfer properties of sCO_2 T-C-P flow without delving into exploring the influencing factors and dynamics governing the initial position of T-C-P flow. Given that the high-speed rotation of the turbine shaft induces a Taylor number as high as 10^{12} in sCO_2 T-C-P flow, it invariably triggers the generation of a substantial number of Taylor vortices, subsequently leading to undesirable impacts and vibrations on the turbine shaft. Therefore, it becomes imperative to meticulously investigate the transition characteristics of Taylor vortices within sCO_2 T-C-P flow and implement measures to suppress the occurrence of Taylor vortices to the fullest extent possible.

Employing experimental techniques to investigate the initial position characteristics of T-C-P flow poses unique challenges. On the one hand, the high-pressure

conditions of sCO_2 make practical execution exceedingly challenging. The emergence of Taylor vortices within the turbine shaft fluid complicates the visibility of these vortices during experimentation. Furthermore, the observation and measurement of vortex formation and evolution necessitate advanced optical and imaging technologies, further adding to the experiment intricacy. On the other hand, precise measurement of the T-C-P flow within the high-speed rotating sCO_2 turbine rotating shaft presents significant challenges in determining flow field parameters such as Taylor vortex velocity and vorticity. Additionally, measurement inaccuracies and noise can adversely affect the experimental results, impeding high-precision attainment. In contrast, employing computational fluid dynamics (CFD) numerical simulation methods allows accurate calculation of Taylor vortex formation and evolution under varying conditions. This approach enables a detailed analysis of the initial position of Taylor vortices and permits extensive parameter studies under various conditions and quantitative information about the initial position of Taylor vortices can be acquired more expeditiously. Hence, this paper employs numerical simulation techniques to investigate the determining factors influencing the initial position of Taylor vortex formation in T-C-P flow under high Reynolds and Taylor numbers. This exploration aims to establish a theoretical understanding of the initial position in T-C-P flow before obtaining reliable experimental data. When dealing with extensive datasets derived from simulations and constructing a regression prediction model, matrix nonlinear regression and neural network regression methods [27, 28] outperform conventional regression techniques in their capacity to handle high-dimensional data and capture nonlinear relationships. Given this, this paper employs these methods to develop a predictive model for the initial position of the Taylor vortex. In conclusion, this paper aims to utilize the Matlab programming algorithm to process Fluent-calculated data to establish a model for predicting the initial position in the T-C-P flow of sCO_2. This research offers valuable theoretical insights for the design of the sCO_2 turbine structure.

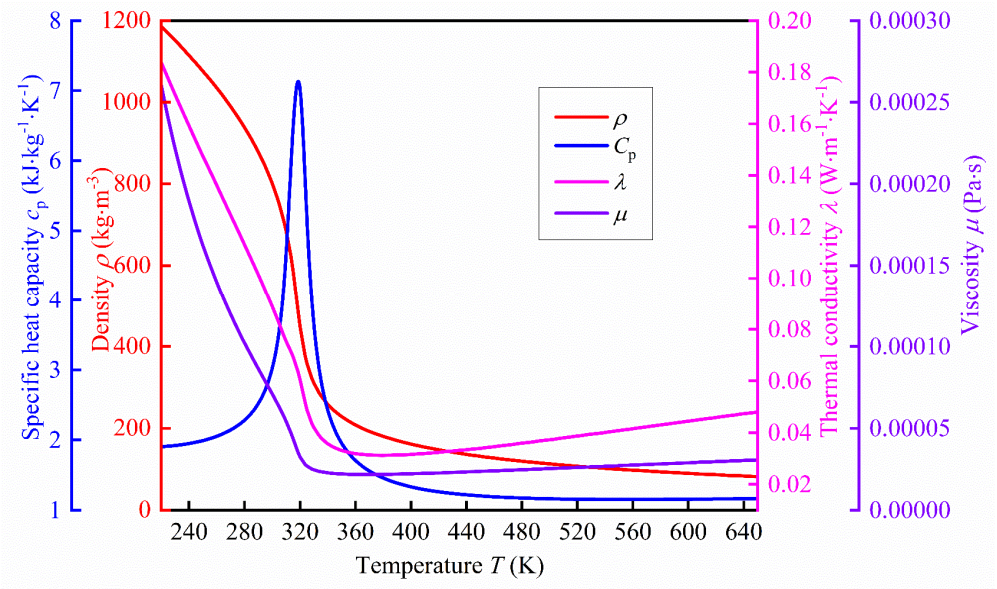

Figure 2. Profile in physical properties of sCO_2 with temperature under 10MPa.

The structural organization of this paper is as follows: Section 2 presents the physical model employed in the study, conducts meshing of the model, validates grid independence, and cross-references existing literature data to corroborate the simulation results. Section 3 delves into examining the impact of the Ta, Re$_a$, Γ, and η on the initial position for T-C-P flow. In Section 4, Fluent software is employed to compute data. Matlab is utilized to develop a computational model program for

determining the initial position, yielding a prediction model for the T-C-P flow initial position.

PHYSICAL MODELS

The schematic illustration in Figure 3 depicts the physical model of a T-C-P flow generated by sCO_2 within a rotating annular gap. In this diagram, R_1 represents the inner radius of the rotating annular gap, which rotates at an angular velocity ω around the z-axis. At the same time, R_2 represents the outer radius of the stationary casing. L stands for the axial length of the annular gap, V_a signifies the axial flow velocity, and δ represents the width of the rotating annular gap. Three essential parameters have been introduced to facilitate the accurate quantitative representation of geometric factors influencing the flow characteristics of T-C-P: radius ratio $\eta = (R_2 - R_1) / R_1$, gap width $\delta = R_2 - R_1$, aspect ratio $\Gamma = L / \delta$.

The axial Reynolds number holds a significant physical significance as it represents the interplay between inertial and viscous forces in the axial flow of sCO_2 within a rotating annular gap. The formula for calculating the axial Reynolds number is defined as follows:

$$Re_a = \frac{V_a D_h}{\nu} \tag{1}$$

The Taylor number holds significance in fluid mechanics as it represents the ratio between centrifugal and viscous forces generated during the rotation and flow of sCO_2 within a rotating annular gap. The precise expression for calculating the Taylor number is defined as follows:

$$Ta = \frac{\omega^2 R_1 (D_h / 2)^3}{\nu^2} \tag{2}$$

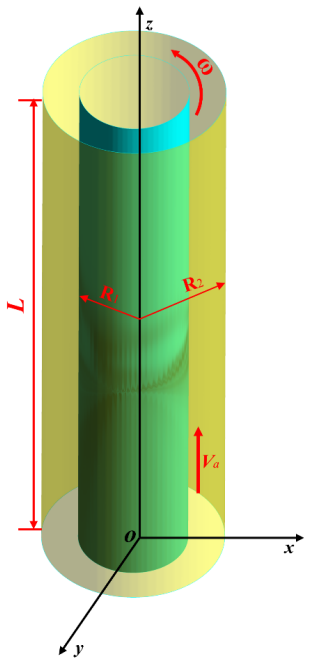

Figure 3. Schematic diagram of the physical model of T-C-P flow.

Given the compact structure design of the sCO_2 turbine, we adopt the rotor diameter from Swann et al. [11]. Thus, we define the rotor radius R_1 as 12.5 mm[11]. Meeting the exact casing assembly requirements, the annular gap width dimension usually falls within the 0.2 to 10 mm range. The value of R_2 varies with changes in the annular gap width. The rotor axial length typically varies between 25 and 150 mm. The physical properties of sCO_2 were computed using the NIST REFPROP physical

property database[29].

CALCULATION SETUP AND BOUNDARY CONDITIONS

The software employed for computational fluid dynamics simulations is Fluent[30].To strike a balance between simulation cost and calculation precision, the Reynolds-averaged equation has been selected as the governing equation for the simulation [25].

$$\frac{\partial(\rho V_j)}{\partial x_j} = 0 \tag{3}$$

$$\frac{\partial(\rho V_i V_j)}{\partial x_j} = -\frac{\partial P}{\partial x_i} + \frac{\partial}{\partial x_j}[\mu_e(\frac{\partial V_i}{\partial x_j} + \frac{\partial V_j}{\partial x_i})] - \frac{\partial}{\partial x_i}(\frac{2}{3}\mu_e \frac{\partial V_j}{\partial x_j}) \tag{4}$$

$$\frac{\partial}{\partial x_i}(\rho V_i h) = \frac{\partial}{\partial x_i}[(\lambda + \frac{C_p \mu_t}{Pr_t})\frac{\partial T}{\partial x_i}] \tag{5}$$

The k-ω SST model was chosen to close equations[7, 25, 31, 32]. The pressure-velocity coupling adopts a robust Couple algorithm. The pressure, momentum, and energy equations utilize the second-order upwind formula with high precision in calculations [30].The residuals have been set as 10^{-6}. The outlet flow and residual curves were closely monitored during the iterative calculation process. Once the curves stabilized and reached the convergence criteria, the entire simulation was considered to have reached convergence conditions, and the calculated values at this time were selected for analysis.

Figure 4 illustrates the computational domain. The outer wall of the rotor shaft serves as a rotating boundary, with the inner casing wall playing a stationary adiabatic role. The sCO_2 fluid flows within the annular gaps created by the revolving shaft and the immobile casing. The turbine shaft, designed for megawatt-level operation, rotates around a fixed axis at an angular velocity denoted as ω. The specific parameter configurations used in the simulation calculations are detailed in Table 3. Given the high operational requirements of the megawatt-level sCO_2 turbine shaft, specific parameters were defined:

The shaft rotation speed is constrained to 0 ~50000 RPM.
The outlet pressure is set at 7/10 MPa.
The inlet temperature fluctuates between 90°C ~110°C.

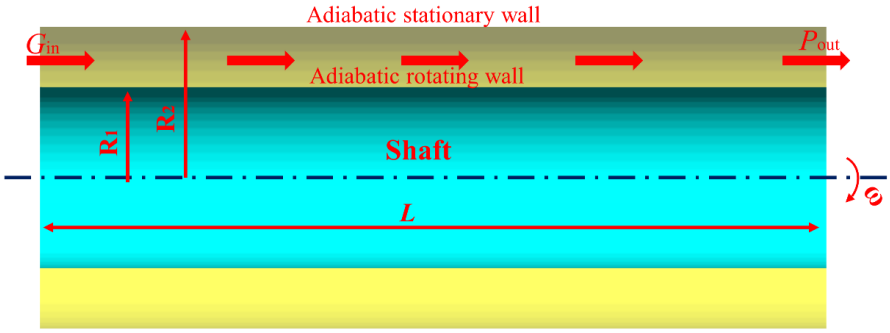

Figure 4. Schematic diagram of computational domain.

GRID INDEPENDENCE AND NUMERICAL SIMULATION RELIABILITY VERIFICATION

ICEM is used to partition the structured mesh of the model illustrated in Figure 3. The resulting grid, depicted in Figure 5, emphasizes mesh refinement near the rotating and stationary walls to ensure a y^+ value of 1 or less.

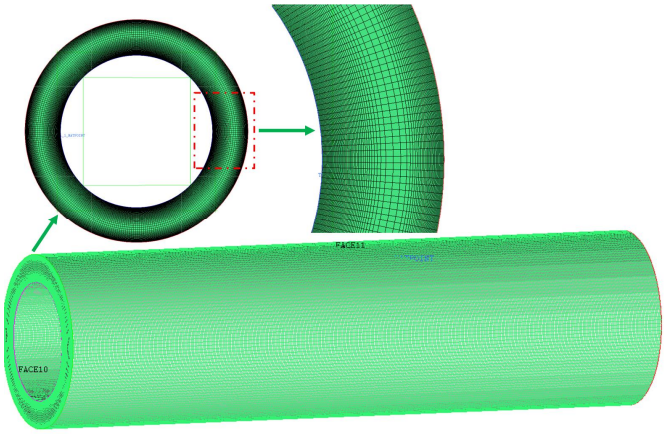

Figure 5. Schematic diagram of mesh division.

To mitigate the influence of the grid numbers on the calculation results, we performed grid independence validation across five sets with diverse grid resolutions. Based on the model parameters and experimental conditions utilized in Swann et al. [11], the simulation employs the parameters outlined in Table 1, and the computed *Nu* during the simulation is illustrated in Figure 6. As shown in Figure 6, the average errors between simulated *Nu* when the number of grids is 390×10^4, 520×10^4, and 573×10^4 are 1.87% and 0.74%, respectively. The simulation calculation opts for a grid number of 573×10^4 to meet accuracy criteria while minimizing computational time.

Table 1. Model parameters and calculation conditions [11]

Parameter	Value
R_1	12.5mm
Annulus height	4mm
L	136mm
ω	0~25000RPM
T_s	50~150℃
sCO_2 temperature	50℃
sCO_2 pressure	10MPa
sCO_2 Mass Flow	0.015kg/s~0.24kg/s

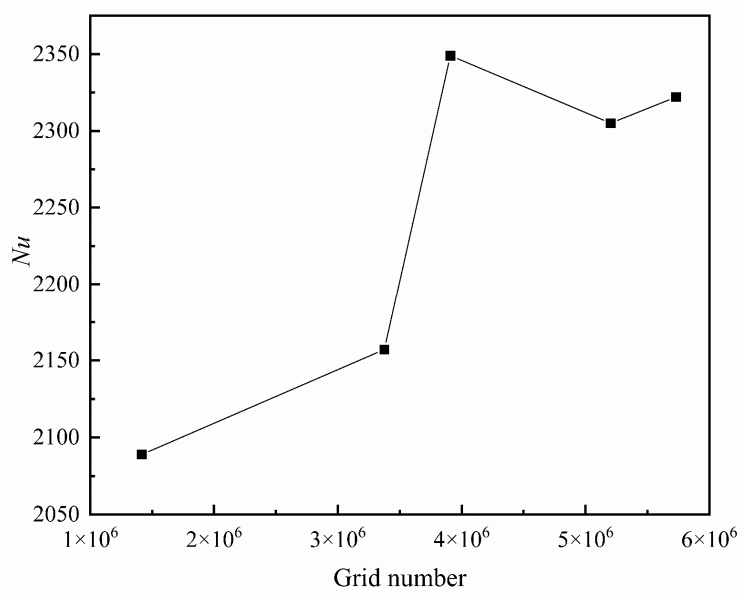

Figure 6. Grid independence verification.

Swann et al.[11] used experimental data to summarize the correlation of *Nu* under 10MPa working conditions：

$$Nu = 8.2 \times 10^{-3} Re_{eff}^{0.84} \tag{6}$$

$$Re_{eff} = \frac{\sqrt{V_a^2 + V_w^2}\,\rho D_h}{\mu} \tag{7}$$

To validate the dependability of the numerical simulation algorithm employed, we utilize the model parameters and boundary conditions detailed in Table 1. We operate four distinct algorithms to compare the computed *Nu* against the *Nu* derived from the formula (6) outlined in the experimental data. The comparative results are enumerated in Table 2.

Table 2. Numerical simulation algorithm reliability verification (*Nu*)

T_s /K	Formula (6) Calculated	k-ω SST		k-ω Standard		k-ε RNG		k-ε Realizable	
		Simulation	error %	Simulation	error %	Simulation	error %	Simulation	error %
343.15	2418.13	2322.37	-3.96	2245.05	-7.16	2209.76	-8.62	2330.21	-3.64
353.15	2201.70	2249.60	2.18	2157.27	-2.02	2124.85	-3.49	2129.23	-3.29

Based on the data presented in Table 2, when operating at a pressure of 10MPa and with varying temperatures of the rotating shaft, it is observed that, in comparison to other turbulence models, the error between *Nu* value calculated using k-ω SST and *Nu* computed using equation (6) is within ±10%. Hence, we can conclude that the chosen k-ω SST computational model is dependable for our numerical simulations.

RESULTS AND DISCUSSION

Characteristics of Taylor Vortex formed by sCO_2

Figures 7 and 8 depict contours illustrating axial and radial velocity distributions (with a mass flow rate of 0.008kg/s) at a rotational speed of 200rad/s. Analyzing the axial velocity distribution in Figure 7, it is evident that Poiseuille flow fails to generate Taylor vortices across the entire cross-section. In the inlet section, the velocity undergoes a gradual transition from the wall towards the center of the cross-section. In contrast, with T-C flow, Taylor vortices emerge at the inlet and uniformly propagate downstream. The stability of T-C-P flow in the inlet section is maintained by the axial flow, mitigating the development of Taylor vortices. However, as the axial distance increases, propelled by the pressure differential between the inner and outer walls and the centrifugal force generated by the rotation of the inner wall, the sCO_2 flow within the rotating annular gap becomes unstable, leading to the formation of a Taylor vortex.

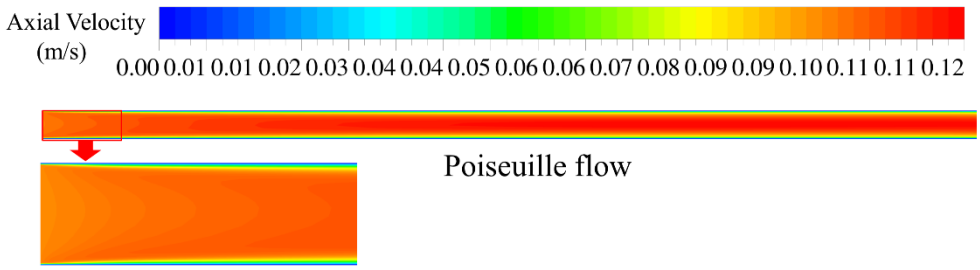

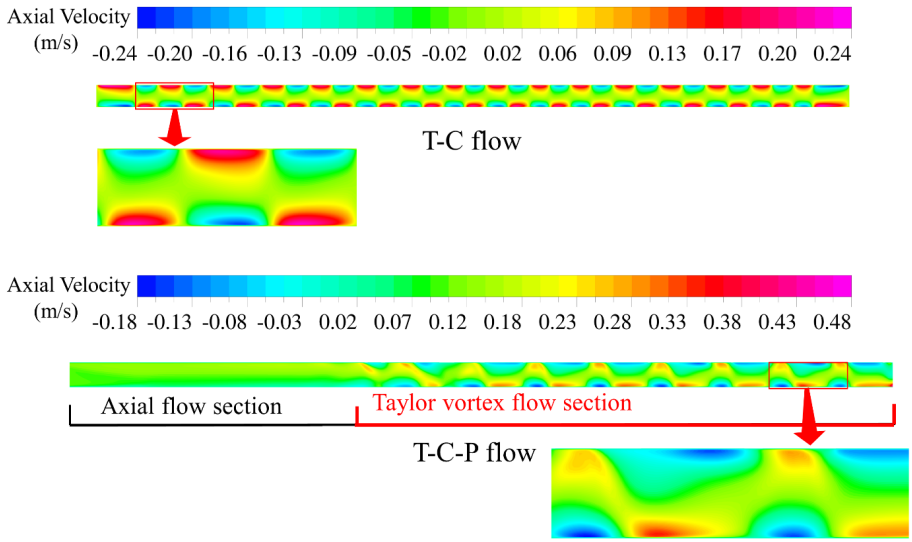

Figure 7. Axial velocity contours of different flows at X=0 in the YOZ plane.

The radial velocity distribution exposes distinct features of the Taylor vortices induced by the sCO_2 T-C flow. These vortices are meticulously organized within the cross-sectional area, exhibiting a periodic alteration between positive and negative radial velocity values. The resulting Taylor vortex configuration is oriented along the radial axis, manifesting an elliptical pattern with a central core and an outward extension along the vortex core. The sCO_2 fluid exhibits varying velocities within this vortex structure. The core at the center experiences rapid fluid motion, giving rise to a high-speed vortex core region, gradually diminishing as it moves from the core towards the periphery. In contrast, the velocity near the boundary of the Taylor vortex is relatively slow, eventually approaching zero. This velocity distribution vividly illustrates the rotational movement of the sCO_2 fluid within the Taylor vortices, depicting the vortex motion. In the case of T-C-P flow, axial flow prevents the formation of a Taylor vortex structure in the inlet section. However, as the sCO_2 flows further along its path, a vortex structure gradually emerges, characterized by a tilted configuration.

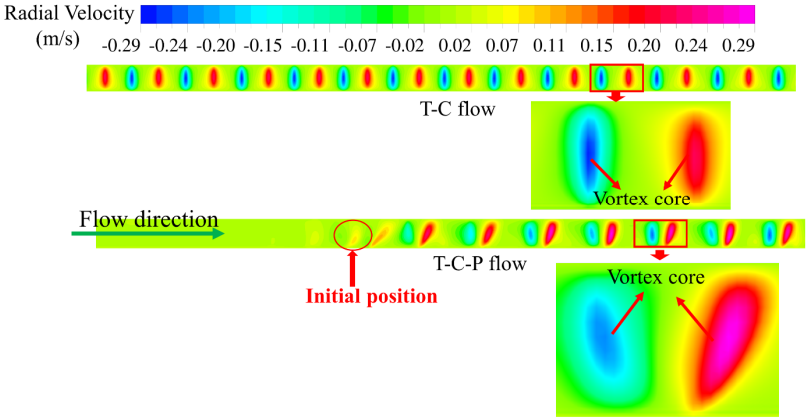

Figure 8. Radial velocity contours of different flows at X=0 in the YOZ plane.

Figure 9 depicts the streamlines comparison between the T-C and T-C-P flow. In the case of T-C flow, the streamlines create numerous concentric annular closed patterns, giving rise to multiple distinct annular vortex structures. Within these vortexes, the fluid circulates circumferentially, spiraling between the rotating and stationary walls. The outer walls also interact, resulting in a circumferential spiral flow. Conversely, for the T-C-P flow, the streamlines are influenced by the rotating wall and the Poiseuille flow, leading to the apparent formation of a single spiral vortex. This two-dimensional spiral flow occurs along the axis and between the inner and outer walls during

circumferential rotation.

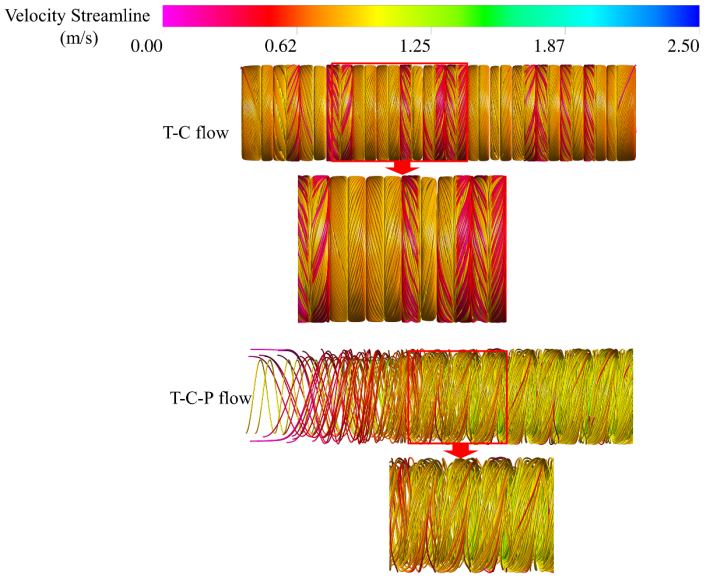

Figure 9. Comparison of streamlines between T-C flow and T-C-P flow.

Research on factors affecting the initial position of the Taylor vortex

In the constantly rotating annular gap, the Taylor vortex's initial position is where the first Taylor vortex emerges during an unstable secondary flow. This is depicted in Figure 8 on the radial velocity contours, showing where the first clear vortex emerges. One of its defining characteristics, as illustrated in Figure 10, is that along the axial flow direction, the radial velocity typically undergoes periodic fluctuations, alternating between positive and negative values. The initial position of the Taylor vortex is the initial position when these alternating periodic changes in radial velocity begin or when the first continuous oscillations between positive and negative radial velocities occur. In determining the location of this initial position of the Taylor vortex, it is selected by taking a comprehensive look at the radial velocity distribution contours and the profile of radial velocity fluctuations.

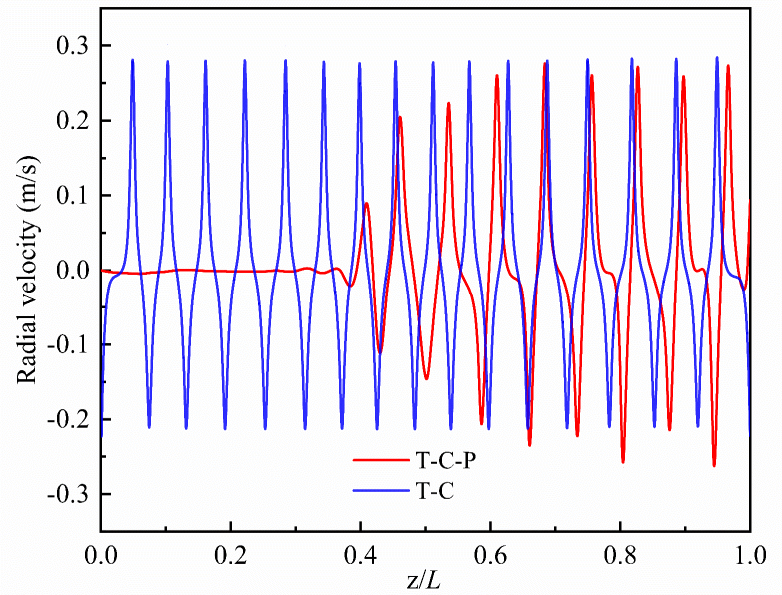

Figure 10. Comparison of radial velocity fluctuation profiles of T-C/T-C-P flow.

To investigate the evolving characteristics of the Taylor vortex initial position in smooth wall conditions concerning variations in inlet flow rate, rotational speed, aspect ratio,

and radius ratio and to formulate a comprehensive understanding of the governing principles, we established four distinct sets of analog number, as detailed in Table 3. Throughout these simulations, the radius of the rotating wall, sCO_2 inlet temperature, and working pressure remain constant. However, the inlet flow rate (converted into Re_a), Ta, Γ, and η （Precisely, only the gap width was adjusted, while other parameters, such as length, axial flow velocity, and rotation speed remain constant） were altered. Table 3 lists the values and ranges of parameters.

Table 3. Detailed parameter setting table

Analog number	1	2	3	4
R_1	12.5mm			
R_2	16.5mm	16.5mm	13.75mm~21mm	16.5mm
T_{in}	110℃			
P	10MPa			
Re_a	$6.6\times10^3 \sim 2.0\times10^5$	9.6×10^4	$3.0\times10^4 \sim 2.0\times10^5$	9.6×10^4
Ta	5.48×10^{11}	$0\sim1.52\times10^{12}$	$3.3\times10^{10} \sim 6.24\times10^{12}$	7.04×10^{11}
η	0.32	0.32	0.11~0.67	0.32
r	34	34	16~108	16~99

The effect Re_a on the initial position of the Taylor vortex

Based on the analog number 1 condition in Table 3, the geometric model utilized for this simulation remains constant. By calculation formula (1) for the Re_a, altering the inlet flow rate means adjusting the Re_a. When the inlet flow rate is raised, Re_a correspondingly increases. This results in a shift of the Taylor vortex initial position, as depicted in Figure 11. This observation is further corroborated by the axial velocity contours at X=0 in the YOZ plane, as seen in Figure 12. When the Re_a is low, the initial position of Taylor vortices near the inlet of the flow channel. This occurs due to a combination of factors. Firstly, the inertial forces are relatively weak, while the viscous forces are comparatively strong. In addition, the sCO_2 fluid is subject to significant centrifugal effects due to the rotation of the inner wall. The axial flow velocity exceeds the axial velocity component of the Taylor vortex, effectively suppressing the formation of the Taylor vortex. Simultaneously, the robust viscous forces make the fluid more susceptible to dissipation within the rotating annular gap. This viscous dissipation leads to the gradual dissipation of energy, resulting in a reduction in vortex intensity. Consequently, the development of Taylor vortices progresses from a densely packed formation to a more sparsely distributed uniform pattern along the flow direction. In this scenario, the dominant force shaping the flow is the centrifugal force from the rotation, leading to a weakened flow stability of sCO_2 in the rotating annular gap.

As the Re_a increases, the axial flow within the rotating annular gap strengthens, and the initial position of the Taylor vortex shifts closer to the outlet of the flow channel. Since the Taylor vortex commences formation near the outlet, it has limited space to develop fully. The Taylor vortices are densely distributed at this stage.

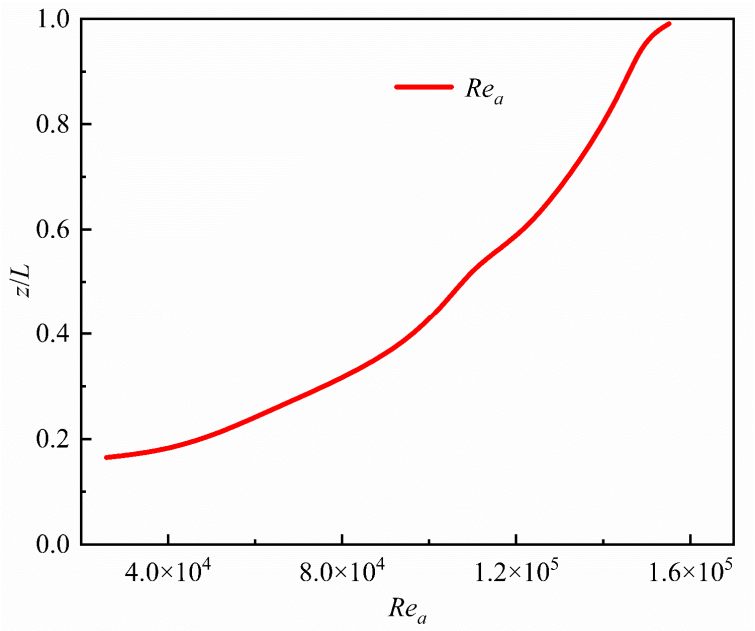

Figure 11. Taylor vortex initial position changes with Re_a

This demonstrates that boosting the inlet flow rate of the T-C-P flow can enhance the stability of the flow within the rotating annular gap and effectively inhibit the formation of Taylor vortices in this configuration.

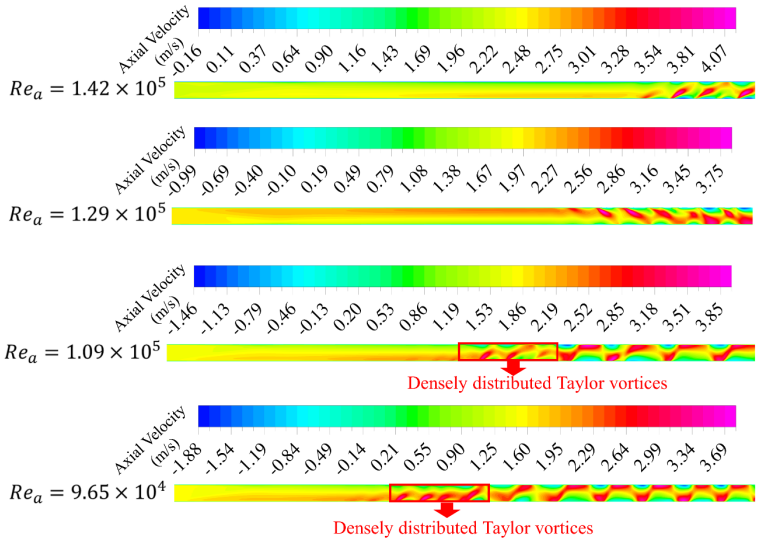

Figure 12. Taylor vortex axial velocity contours at X=0 in the YOZ plane at different Re_a

The effect of Ta on the initial position of the Taylor vortex

Based on the analog number 2 condition in Table 3, various inner wall rotation speeds have been established to investigate and analyze the influence of Ta on the initial position of the Taylor vortex. Figures 13 and 14 depict the profile curves of the Taylor vortex initial position with varying Ta and the radial velocity contours at X=0 in the YOZ plane for Ta values of 3.22×10^{11}, 4.44×10^{11}, 5.85×10^{11}, and 7.46×10^{11}. As the Ta increases, the centrifugal effect of the rotating inner wall on sCO_2 is enhanced, and the initial position of the Taylor vortex gradually approaches the inlet of the annular gap. Based on the distinctive radial velocity contours of Taylor vortices formed under various Ta conditions, it becomes evident that the inner wall rotational centrifugal force propels the sCO_2 fluid towards the outer wall. Simultaneously, due

to the impact of axial flow, the resulting Taylor vortex exhibits an oblique distribution aligned with the direction of the flow. The Taylor vortex is influenced by two primary factors, namely wall rotation and axial motion, due to the presence of axial flow. The impact of the process is particularly pronounced near the rotating wall, leading to the formation of an apparent vortex on that side. The radial velocity, driven by the centrifugal force, propels the fluid away from the center of rotation, resulting in a vigorous radial motion. Consequently, this fluid portion manifests a distinct Taylor vortex along one side of the rotating wall. In contrast, near the stationary boundary, the effect of rotation is diminished, while the influence of axial flow becomes more prominent. Axial flow directs the fluid toward its flow, thereby suppressing radial motion. As a result, the Taylor vortex on the fixed wall side exhibits a larger shape than the Taylor vortex on the rotating side at the YOZ section.

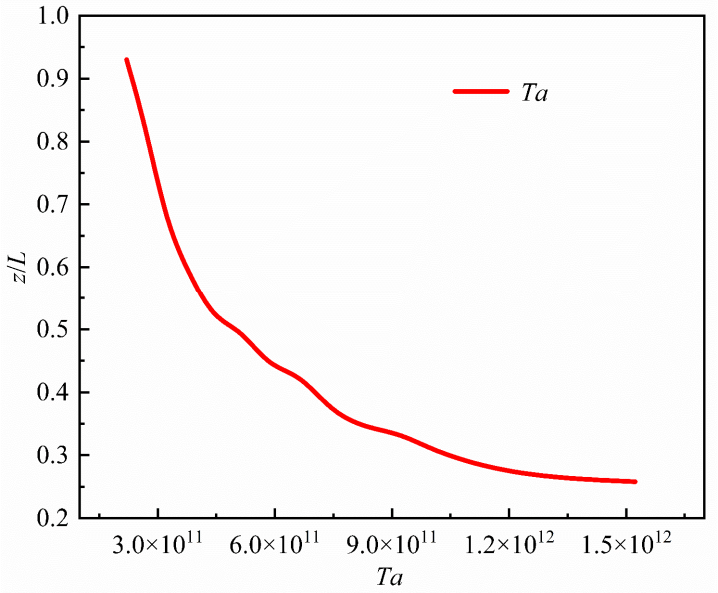

Figure 13. Taylor vortex initial position changes curve with *Ta*

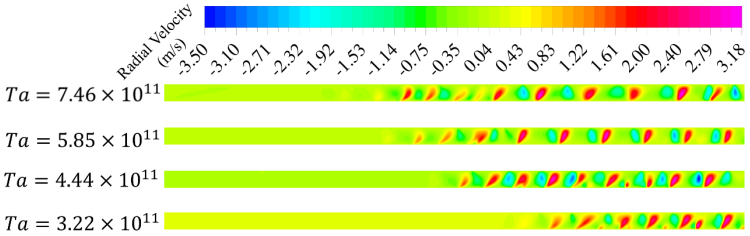

Figure 14. Radial velocity contours at X=0 in the YOZ plane at different *Ta*

This demonstrates that elevating the rotational speed of the inner wall results in heightened instability for the T-C-P flow, an augmented quantity of Taylor vortices, and a closer proximity of the initial position of the Taylor vortex to the inlet of the annular gap.

The effect of *η* on the initial position of the Taylor vortex

Based on the analog number 3 condition in Table 3, alter the η to investigate its impact on the initial position of the Taylor vortex. Figures 15 and 16, respectively, show the 3D diagram of the initial position of the Taylor vortex as a function of the η and the axial velocity contours at X=0 in the YOZ plane when the η is 0.11, 0.18, 0.33 and 0.52. Reducing the η means a decrease in the width of the annular gap. With this decreasing η, the fluid, driven by centrifugal force, moves towards the stationary outer wall with a specific radial velocity. This radial velocity gradually diminishes to zero, causing a simultaneous rise in pressure. Due to the narrow gap, significant velocity

and pressure gradients emerge between the inner and outer walls. These gradients facilitate the easier rotation of the sCO_2 fluid, and the initial position of the Taylor vortex moves closer to the inlet of the flow channel. As η increases, the widening of the rotating annular gap is amplified, allowing additional space for the sCO_2 fluid to flow. This, in turn, diminishes the constraining influence of both the inner and outer walls on the movement of the sCO_2 fluid, resulting in a less pronounced formation of the Taylor vortex. The vortex exclusively emerges on the side of the rotating wall, with its initial position located nearer to the flow channel outlet, thereby enhancing the stability for T-C-P flow.

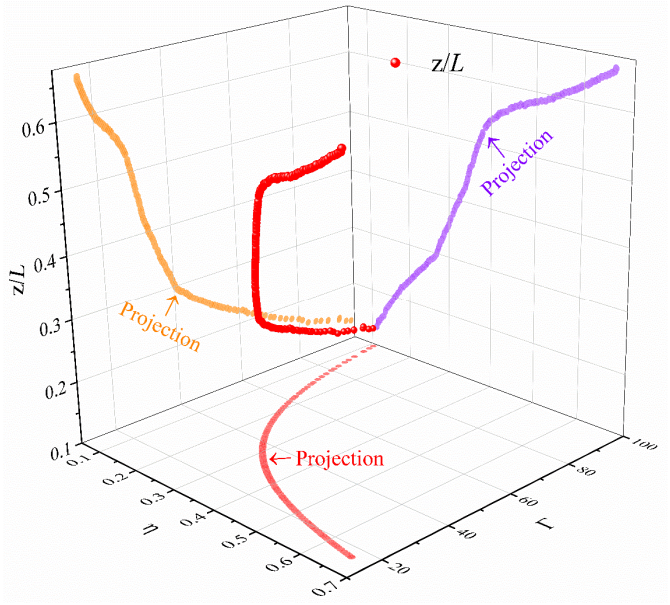

Figure 15. Initial position diagram of Taylor vortex composed of different Γ and *η*

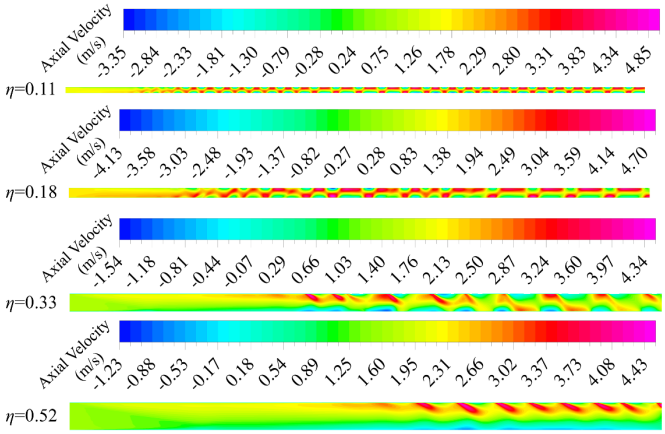

Figure 16. Taylor vortex axial velocity contours at X=0 in the YOZ plane at different *η*

Therefore, keeping the streamwise length of the T-C-P flow constant while maintaining the same axial flow velocity and rotational speed, increasing *η* will effectively suppress the formation of Taylor vortices.

The effect of Γ on the initial position of the Taylor vortex

Based on the analog number 4 condition in Table 3, Modify Γ to investigate its influence on the alteration of the initial position of the Taylor vortex. Figures 17 and 18, respectively, show the Taylor vortex position profile curve with Γ and the axial velocity contours at X=0 in the YOZ plane when the Γ is 20, 22, 43 and 50. As Γ increases, the initial relative position z/L of the Taylor vortex diminishes progressively.

In contrast, the absolute location Z of the Taylor vortex remains virtually constant across various Γ. When Γ reaches 50, the distribution of Taylor vortices experiences a transition from a dense configuration to a sparser one. This occurs due to the heightened influence of viscous forces when sCO_2 fluid flows within a large Γ. Viscous dissipation leads to energy loss, causing a weakening of the vortices, resulting in a gradual decrease in the density of Taylor vortices. Consequently, the distribution of formed Taylor vortices shifts from high vortex density to one characterized by sparser vortices. Conversely, as Γ decreases gradually, the distribution of formed Taylor vortices becomes increasingly uniform.

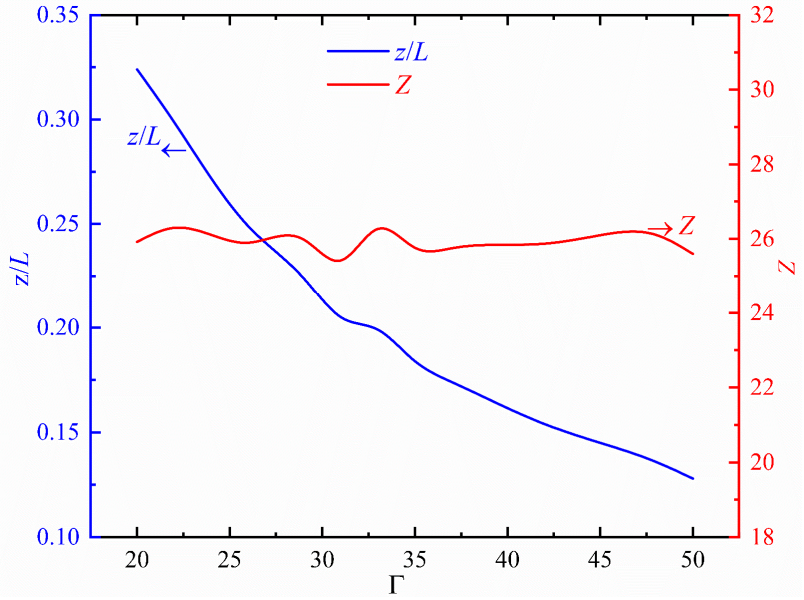

Figure 17. Taylor vortex initial position profile curve with Γ

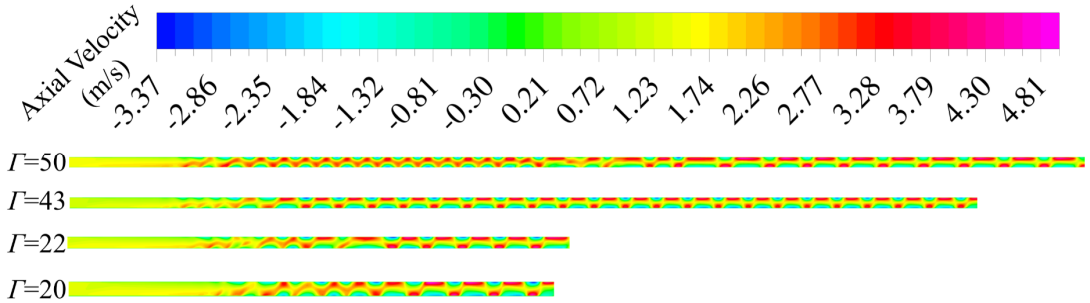

Figure 18. Taylor vortex axial velocity contours at different Γ

Hence, one can infer that a rise in Γ will undermine the stability of the T-C-P fluid flow, thereby bringing the z/L of the Taylor vortex closer to the inlet of the T-C-P flow.

Taylor vortex initial position prediction model

Multivariate matrix exponential regression model construction

Referring to the heat transfer correlations outlined in heat transfer literature [33], the versatility of the power exponential function is widely recognized in engineering. It offers a straightforward parameter interpretation and exhibits robust data-fitting capabilities. To forecast the initial position of the Taylor vortex generated by sCO2 T-C-P flow precisely, it offers valuable insights for determining the structural parameters of the sCO_2 turbine shaft seal. When operating at 10MPa, based on the variable range combinations detailed in Table 3. The correlations for Re_a, Ta, η and Γ were summarized as follows：

$$z/L=ARe_a^{x_1}Ta^{x_2}\eta^{x_3}\Gamma^{x_4} \quad (8)$$

Apply the natural logarithm to both sides of the equation and rearrange it into the following expression:

$$\ln(z/L)=\ln A\cdot\ln e+x_1\ln(Re_a)+x_2\ln(Ta)+x_3\ln(\eta)+x_4\ln(\Gamma) \quad (9)$$

In numerical simulation, a group of (Re_a, Ta, η, Γ) can uniquely determine a z/L. For the numerical simulation conditions, the logarithm with base e forms the matrix B and Y.

$$B=\begin{pmatrix}\ln e & \cdots & \ln((\Gamma)_{14})\\ \vdots & \ddots & \vdots\\ \ln e & \cdots & \ln((\Gamma)_{n4})\end{pmatrix},\quad Y=\begin{pmatrix}\ln((z/L)_{11})\\ \ln((z/L)_{21})\\ \ln((z/L)_{31})\\ \vdots\\ \ln((z/L)_{n1})\end{pmatrix},\quad \text{where } n=560.$$

Take the logarithm of the unknown numbers A, x_1, x_2, x_3, and x_4 with base e to form a matrix $X=(\ln A, x_1, x_2, x_3, x_4)^{\mathrm{T}}$. Bring 560 data points into matrix B, X and Y to form a system of equations [34]:

$$BX=Y \quad (10)$$

At this juncture, the quantity of equation systems exceeds the number of unknown variables by a significant margin ($R(B,Y)\neq R(B)$). The system of equations (9) has no solution [35]. To establish a suitable correlation for predicting the initial position of the Taylor vortex, it becomes imperative to derive a solution for the system of equations. Consequently, this involves identifying a matrix X that minimizes the error between BX and Y to the greatest extent possible.

Define error function E(*X*)

$$E(X)=\sum_{i=1}^{n}[\ln(A)\cdot\ln e+x_1\ln((\mathrm{Re}_a)_{i1})+x_2\ln((Ta)_{i2})+x_3\ln((\eta)_{i3})+x_4\ln((\Gamma)_{i4})-\ln((z/L)_i)]^2$$

, n=560. (11)

To minimize the value of E(X), it is equivalent to finding X such that $E(X)=\|BX-Y\|^2$ smallest [36]，According to linear equations and matrix theory, combined with the characteristics of correlation (9), E(X) can be transformed into:

$$E(X)=\|BX-Y\|^2=(BX-Y)^{\mathrm{T}}\cdot(BX-Y)$$

$$=B^{\mathrm{T}}X^{\mathrm{T}}BX-2B^{\mathrm{T}}X^{\mathrm{T}}Y+YY^{\mathrm{T}} \quad (12)$$

Because E(X) is a function of X, X under the condition of $\frac{\partial E(X)}{\partial X}=0$ minimizes the value of E(X).

$$\frac{\partial E(X)}{\partial X}=2B^{\mathrm{T}}BX-2B^{\mathrm{T}}Y=0 \quad (13)$$

Simplifying to get the least squares solution is

$$X=(B^TB)^{-1}B^TY \quad (14)$$

In the Mtatlab software, by writing a program to solve the above (8) ~ (14) matrix equations [37, 38]，after calculation, the following relationship was obtained:

$$z/L=1.6101129\times10^7(Re_a)^{0.5668}(Ta)^{-0.7452}(\eta)^{2.1828}(\Gamma)^{-0.4028} \quad (15)$$

The applicable scope of correlation 14 is specified in Table 3. Based on equation (14) provided above, one can deduce that to suppress the formation of the Taylor vortex,

specific actions such as enhancing the inlet flow rate and lowering the rotational speed of the shaft can effectively restrain. It is important to note that because equation (14) provides an approximate solution, a discrepancy exists between the Taylor vortex initiation's actual position and the formula's prediction. This discrepancy may be significant at specific locations, rendering the multivariate exponential regression model unsuitable for extensive and high-precision forecasting.

Construction of a Neural Network Model for the Initial Position of the Taylor Vortex

Determination of Taylor vortex initial position by neural network model

The neural network model addresses the limitations of the initial position prediction model (14). Neural network regression prediction leverages deep learning technology to autonomously capture intricate nonlinear relationships from extensive datasets autonomously, rendering it more flexible and accurate than conventional regression prediction techniques [39] [40]. This approach has proven effective in sCO_2 heat transfer [41] and has also been applied to the study of T-C flow[42]. In the neural network model, signals are forward-propagated, and errors are backward-propagated. The input layer of the neural network model comprises Re_a, Ta, Γ, and η, with a fixed count of 4 neurons in this layer. The output layer represents the initial position of the Taylor vortex. We randomly assign 70% of the 560 data sets for the training set, 15% for the validation set, and 15% for the test set. Figure 19 illustrates a schematic representation of the designed structure of the neural network model.

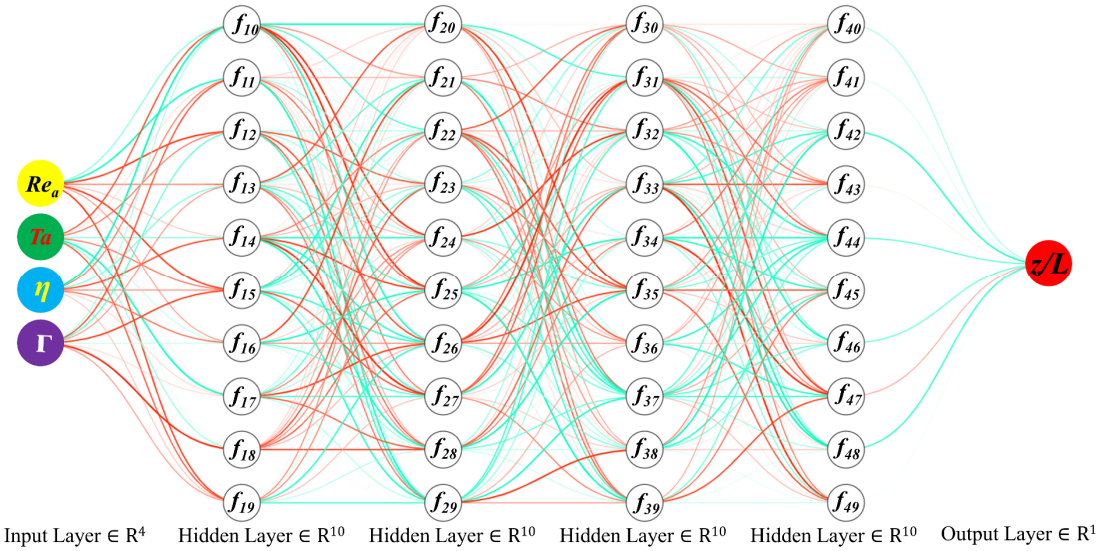

Figure 19. Schematic diagram of Taylor vortex initial position neural network structure.

The Levenberg-Marquardt backpropagation algorithm exhibits excellent convergence characteristics, combining the advantages of the Newton and gradient methods. It yields reliable results, particularly well-suited for training tiny to medium-sized neural networks[43, 44]. Consequently, the Levenberg-Marquardt algorithm has been chosen for computation. The size of the hidden layer plays a crucial role in shaping the neural network model and is determined using the following empirical formula[45].

$$k = \sqrt{p+q} + a \tag{16}$$

Within the range of hidden layers from 6 to 12, the correlation coefficient R was used to determine the appropriate number of hidden layers. After a comprehensive comparison of the R values calculated by the neural network models of different hidden layers, it is found that when the number of hidden layers is set to 10, the predicted variable and the expected variable are the correlation coefficient between

them is closer to 1. For this reason, the hidden layer is selected as 10, and the neural network model established is the 4-10-1 model. The mean square error (MSE) was selected as the performance function to predict the accuracy of the initial position model. MSE represents the average sum of squares of the difference between the predicted value of the initial position and the simulated value, which includes both the variance and the bias. The calculation formula is:

$$MSE = \frac{1}{n}\sum_{i=1}^{n}[(z/L)_i - \widehat{(z/L)_i}]^2 \quad (17)$$

Determination of initial position neural network model parameters

As indicated in Table 4, a feedforward neural network with a regression function is employed. The results reveal a significant nonlinear relationship between the input neurons and the output outcomes. Therefore, the activation function for the hidden layer is the nonlinear hyperbolic tangent S-shaped function known as Tansig. To directly convert the output values into the initial position for predictive purposes, the activation function for the output layer is selected to be the linear transmission Purelin function. The combination of Tansig-Purelin offers rapid training and a reduced risk of overfitting and is particularly well-suited for regression prediction. Set the iteration limit to 10,000 and the performance threshold to 0.0001. The configuration of the learning rate significantly impacts the training pace and prediction precision of the Taylor vortex initial position neural network model. After experimenting with various learning rates, a value of 0.001 was ultimately chosen [46].

Table 4. Taylor vortex initial position neural network prediction model settings

Parameter	Set up
neural network model	feedforward backpropagation
number of iterations	10000
performance value	0.0001
learning rate	0.001[47]
algorithm function	Levenberg-Marquardt
transfer function	Tansig-Purelin[48, 49]
performance function	MSE

Initial position neural network model calculation results

A total of 560 datasets were utilized for the training process. Following the 445th iteration cycle, the training and configuration errors stabilized, indicating a converged state. The training program was halted at this point, and Figure 20 depicts the Mean Squared Error (MSE) curve. The established neural network model reached an average error value of 5.3521E-5 at this crucial juncture.

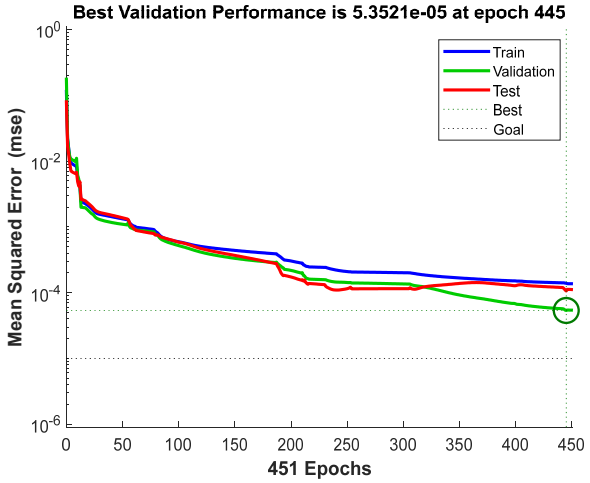

Figure 20. Neural network model training performance profile.

Figure 21 presents the error histogram post-training. The graph shows that the deviation between the output and the target (simulated value) for most data sets is nearly zero. The 4-10-1 neural network model has been established to achieve precise forecasts of initial position. Correlation analyses are separately performed on the training, validation, and test datasets. Four sets of linear regression plots are displayed in Figure 22. Figure 22 displays four sets of linear regression plots, revealing a close alignment of data points with the regression line. Specifically, the R for the training dataset is 0.99849, the validation dataset is 0.9995, and the test dataset is 0.99854. Cumulatively, the R-value across all datasets is 0.99867, demonstrating the accurate initial position prediction capability of the established 4-10-1 neural network model.

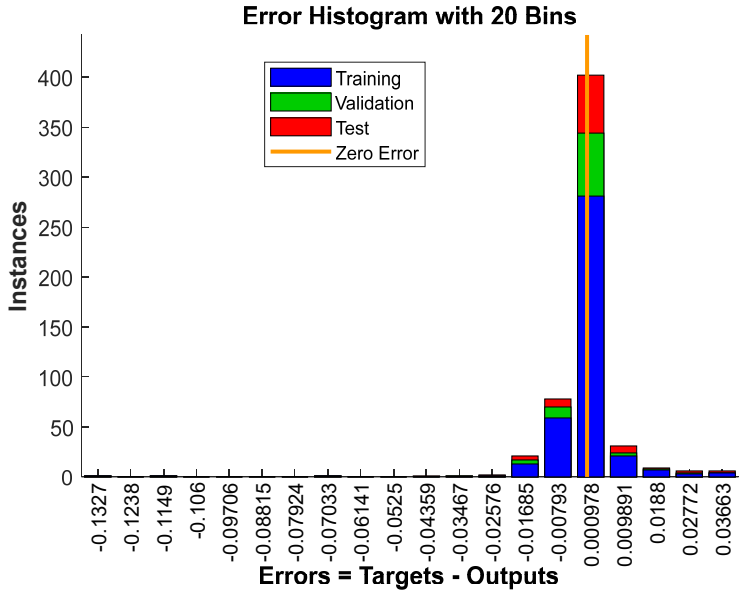

Figure 21. Taylor vortex initial position prediction model error histogram.

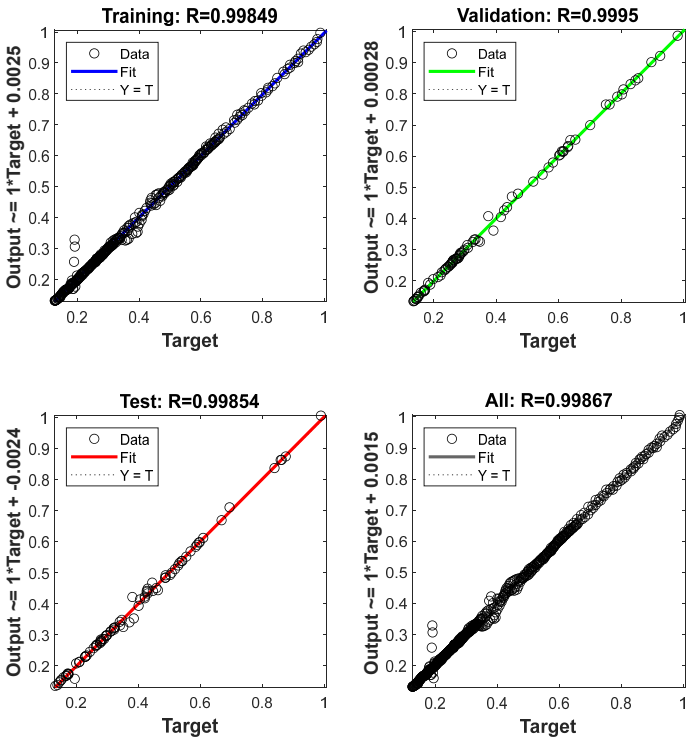

Figure 22. Correlation coefficient diagram of data set.

Comparative analysis of Taylor vortex initial position prediction models

To assess and compare the predictive accuracy of the multivariate exponential regression model for the initial position and the neural network model, we adhered to the parameter design conditions outlined in Table 5. We then contrasted the forecasted values produced by the established multivariate matrix exponential regression model for the initial position and the neural network model with the simulated values, as illustrated in Figure 23. Evidently, the neural network model closely aligns with the simulated values, exhibiting errors of less than 10%. Within the range of initial positions from 0.2 to 0.4, the discrepancy between the predicted values from the multivariate matrix exponential regression model and the simulated values remains within the 10% margin. However, at other relative positions, the disparity between the predicted and simulated values of the initial position regression model is considerably more pronounced. Therefore, the optimal model for predicting the initial position of the Taylor vortex is the established 4-10-1 neural network model.

Table 5. Parameter settings

Parameter	Value
R_1	12.5mm
R_2	16.5mm
T_{in}	110℃
P	10MPa
ω	14000RPM~50000RPM
η	0.11~0.66
r	16~99

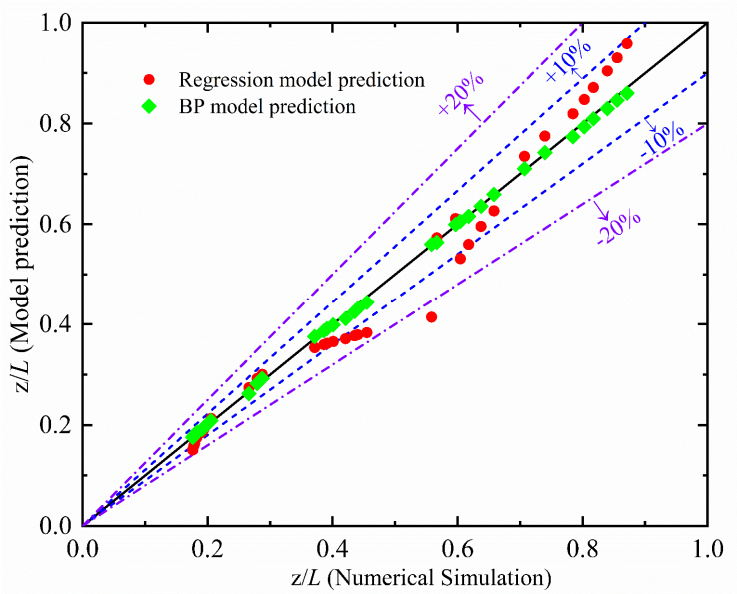

Figure 23. Comparison of initial position prediction values for different model.

CONCLUSIONS

This paper presents a comprehensive calculation and analysis of the initial position in the Taylor vortex, which is generated by the flow of sCO_2 within the turbine shaft and casing. The primary findings can be summarized as follows:

（1） sCO_2 exhibits a typical T-C-P flow pattern within the turbine shaft and casing. Compared with the T-C flow, due to the influence of axial flow, the T-C-P flow includes a stable flow section and a Taylor vortex section; the Taylor vortex distribution formed by the T-C flow has a central core and extends outward along the vortex core. Taylor vortex distribution formed by T-C-P flow presents

a structurally oblique vortex.

（2） The generation of the Taylor vortex can be suppressed, and the stability of T-C-P flow improved by increasing the flow rate, reducing the rotational speed, increasing the radius ratio, and reducing the aspect ratio.

（3） A matrix nonlinear regression model and a 4-10-1 feedforward neural network model for predicting the Taylor vortex initial position were established with the Matlab program. A comparative analysis of the two models found that the matrix nonlinear regression model prediction accuracy is lower than the prediction accuracy of the 4-10-1 feedforward neural network model. The prediction accuracy of the 4-10-1 feedforward neural network model for the initial position is within 10%.

ACKNOWLEDGMENTS

The authors thank the National Natural Science Foundation of China (Grant No. 52176090) and the Chinese Academy of Sciences for their support through the Youth Team Support Plan in Basic Research (Grant No. YSBR-043). Thanks to the Major national science and technology infrastructure “High-Efficiency and Low-Carbon Gas Turbine Research Facility” (2017-000052-73-01-001569).

Nomenclature

Re_a	Axial Reynolds number	Ta	Taylor number
R_1	Shaft radius	R_2	Casing radius
L	Axial length of rotating shaft	V_a	Inlet velocity
D_h	Hydraulic diameter	ω	Shaft rotation speed
V_w	Velocity of the rotating wall	v	Kinematic viscosity of sCO_2
μ	Viscosity of sCO_2	η	Radius ratio
Γ	Aspect ratio	δ	Annular gap width
n	Sample size	MSE	Mean square error
k	Hidden layer size	p	Number of input layer nodes
q	Number of output layer nodes	Re_{eff}	Effective Reynolds number
Nu	Nusselt number	P	Pressure
λ	Thermal conductivity of sCO_2	C_p	Specific heat capacity of sCO_2
ρ	Density of sCO_2	T_{in}	sCO_2 inlet temperature
T_s	Shaft temperature	RPM	Revolutions Per Minute
T-C-P	Taylor-Couette-Poiseuille	T-C	Taylor-Couette

a Adjustment constant in the range of 1 ~10

$(z/L)_i$ Numerical simulation value

$(\widehat{z/L})_i$ Predicted value of the neural network model

REFERENCES

[1] P. Wu, Y. Ma, C. Gao, W. Liu, J. Shan, Y. Huang, J. Wang, D. Zhang, X. Ran, A review of research and development of supercritical carbon dioxide Brayton cycle technology in nuclear engineering applications, Nuclear Engineering and Design, 368 (2020) 110767.

[2] Y. Liu, Y. Wang, D. Huang, Supercritical CO2 Brayton cycle: A state-of-the-art review, Energy, 189 (2019) 115900.

[3] J. Chen, L. Liu, G. Liao, F. Zhang, E. Jiaqiang, S. Tan, Design and off-design performance analysis of supercritical carbon dioxide Brayton cycles for gas turbine waste heat recovery, Applied Thermal Engineering, 235 (2023) 121295.

[4] W.-L. Cheng, W.-X. Huang, Y.-L. Nian, Global parameter optimization and criterion formula of supercritical carbon dioxide Brayton cycle with recompression, Energy Conversion and Management, 150 (2017) 669-677.

[5] A. Narasimhan, R. Kamal, E. Almatrafi, Novel synergetic integration of supercritical carbon dioxide Brayton cycle and adsorption desalination, Energy, 238 (2022)

121844.
[6] Q. Du, L. Zhang, D. Zhang, Y. Xie, Numerical investigation on flow characteristics and aerodynamic performance of shroud seal in a supercritical CO2 axial-flow turbine, Applied Thermal Engineering, 169 (2020) 114960.
[7] J. Chen, C. Guo, Y. Jiang, Y. Sun, C. Guo, Numerical investigation of flow and heat transfer characteristics of supercritical CO2 in high-speed rotating annulus, Heat Transfer Research, 52(12) (2021) 67-95.
[8] J. Moore, M. Day, S. Cich, D. Hofer, Testing of a 10 MWe supercritical CO2 turbine, in: Proceedings of the 47th Turbomachinery Symposium, Turbomachinery Laboratory, Texas A&M Engineering Experiment Station, 2018.
[9] J. Moore, S. Cich, M. Day-Towler, J. Mortzheim, Development and testing of a 10 MWe supercritical CO2 turbine in a 1 MWe flow loop, in: Turbo Expo: Power for Land, Sea, and Air, American Society of Mechanical Engineers, 2020, pp. V011T031A018.
[10] P.B. Swann, H. Russell, I.H. Jahn, Taylor-Couette-Poiseuille flow heat transfer in a high Taylor number test rig, Journal of the Global Power and Propulsion Society, 5 (2021) 126-147.
[11] P. Swann, I. Jahn, H. Russell, Supercritical carbon dioxide Taylor–Couette–Poiseuille flow heat transfer, International Journal of Heat and Mass Transfer, 183 (2022) 122204.
[12] G.I. Taylor, Stability of a viscous liquid contained between two rotating cylinders, Proceedings of the Royal Society of London Series a-Containing Papers of a Mathematical and Physical Character, 102(718) (1923) 541-542.
[13] R. Ostilla-Mónico, R. Verzicco, D. Lohse, Effects of the computational domain size on direct numerical simulations of Taylor-Couette turbulence with stationary outer cylinder, Physics of Fluids, 27(2) (2015).
[14] L. Hu, Q. Deng, J. Li, Z. Feng, Model improvement for shaft-type windage loss with CO2, The Journal of Supercritical Fluids, 190 (2022) 105747.
[15] C.D. Andereck, S.S. Liu, H.L. Swinney, Flow regimes in a circular Couette system with independently rotating cylinders, Journal of Fluid Mechanics, 164 (1986) 155-183.
[16] J. Kaye, E.C. Elgar, Modes of Adiabatic and Diabatic Fluid Flow in an Annulus With an Inner Rotating Cylinder, Transactions of the American Society of Mechanical Engineers, 80(3) (2022) 753-763.
[17] P.S. Marcus, Simulation of Taylor-Couette flow. Part 2. Numerical results for wavy-vortex flow with one travelling wave, Journal of Fluid Mechanics, 146 (1984) 65-113.
[18] N. Gravas, B. Martin, Instability of viscous axial flow in annuli having a rotating inner cylinder, Journal of Fluid Mechanics, 86(2) (1978) 385-394.
[19] L.A. Bordag, O. Chkhetiani, M. Fröhner, V. Myrnyy, Interaction of a rotational motion and an axial flow in small geometries for a Taylor–Couette problem, Journal of fluids and structures, 20(5) (2005) 621-641.
[20] S.T. Wereley, R.M. Lueptow, Velocity field for Taylor–Couette flow with an axial flow, Physics of Fluids, 11(12) (1999) 3637-3649.
[21] J.-Y. Hwang, K.-S. Yang, Numerical study of Taylor–Couette flow with an axial flow, Computers & Fluids, 33(1) (2004) 97-118.
[22] H. Abou-Ziyan, R. Ameen, K. Elsayed, Fluid flow and convection heat transfer in concentric and eccentric cylindrical annuli of different radii ratios for Taylor-Couette-Poiseuille flow, Advances in Mechanical Engineering, 13(8) (2021) 16878140211040731.
[23] Y. Matsukawa, T. Tsukahara, Subcritical transition of Taylor−Couette−Poiseuille flow at high radius ratio, Physics of Fluids, 34(7) (2022).
[24] A. Gavrilov, Y. Ignatenko, Numerical Simulation of Taylor—Couette—Poiseuille Flow at Re = 10,000, Fluids, 8(10) (2023) 280.

[25] K. Qin, D. Li, C. Huang, Y. Sun, J. Wang, K. Luo, Numerical investigation on heat transfer characteristics of Taylor Couette flows operating with CO2, Applied Thermal Engineering, 165 (2020) 114570.
[26] P.B. Swann, H. Russell, I. Jahn, Rotating shaft thermal analysis for supercritical carbon dioxide radial inflow turbines, in: 15th International Energy Conversion Engineering Conference, 2017, pp. 4864.
[27] E. Kocak, E. Aylı, H. Turkoglu, A comparative study of multiple regression and machine learning techniques for prediction of nanofluid heat transfer, Journal of Thermal Science and Engineering Applications, 14(6) (2022) 061002.
[28] J. Kim, C. Lee, Prediction of turbulent heat transfer using convolutional neural networks, Journal of Fluid Mechanics, 882 (2020) A18.
[29] E.W. Lemmon, M.L. Huber, M.O. McLinden, NIST standard reference database 23, Reference fluid thermodynamic and transport properties (REFPROP), version, 9 (2010).
[30] I. ANSYS, ANSYS FLUENT user's guide, Canonsburg, PA, 15317 (2011).
[31] A. Ding, X. Ren, X. Li, C. Gu, Numerical investigation of static characteristic of a tilting-pad journal bearing using shear stress transport model and air backflow, Advances in Mechanical Engineering, 11(4) (2019) 1687814019841816.
[32] X. Liu, X. Xu, C. Liu, J. Ye, H. Li, W. Bai, C. Dang, Numerical study of the effect of buoyancy force and centrifugal force on heat transfer characteristics of supercritical CO2 in helically coiled tube at various inclination angles, Applied thermal engineering, 116 (2017) 500-515.
[33] G. Nellis, S. Klein, Heat transfer, Cambridge university press, 2008.
[34] J.N. Franklin, Matrix theory, Courier Corporation, 2012.
[35] G. Strang, Introduction to linear algebra, SIAM, 2022.
[36] T.J. Rivlin, Overdetermined Systems of Linear Equations, SIAM Review, 5(1) (1963) 52-66.
[37] D.T. Valentine, B.H. Hahn, Essential MATLAB for engineers and scientists, Academic Press, 2022.
[38] B.R.H.R.L. Lipsman, J.M. Rosenberg, A Guide to MATLAB, 2001.
[39] S. Haykin, Neural networks and learning machines, 3/E, Pearson Education India, 2009.
[40] Y. Song, X. Chen, J. Zhou, T. Du, F. Xie, H. Guo, Research on performance of passive heat supply tower based on the back propagation neural network, Energy, 250 (2022) 123762.
[41] F. Sun, G. Xie, S. Li, An artificial-neural-network based prediction of heat transfer behaviors for in-tube supercritical CO2 flow, Applied Soft Computing, 102 (2021) 107110.
[42] S.-L. Sun, D. Liu, Y.-Z. Wang, H.-B. Kim, M. Hassan, H.-J. Hong, Heat transfer performance prediction of Taylor–Couette flow with longitudinal slits using artificial neural networks, Applied Thermal Engineering, 221 (2023) 119792.
[43] B.M. Wilamowski, H. Yu, Improved Computation for Levenberg–Marquardt Training, IEEE Transactions on Neural Networks, 21(6) (2010) 930-937.
[44] D. Wijayasekara, M. Manic, P. Sabharwall, V. Utgikar, Optimal artificial neural network architecture selection for performance prediction of compact heat exchanger with the EBaLM-OTR technique, Nuclear Engineering and Design, 241(7) (2011) 2549-2557.
[45] R. Reed, R.J. MarksII, Neural smithing: supervised learning in feedforward artificial neural networks, Mit Press, 1999.
[46] P. Arafin, A.M. Billah, A. Issa, Deep learning-based concrete defects classification and detection using semantic segmentation, Structural Health Monitoring, (2023) 14759217231168212.
[47] L.N. Smith, A disciplined approach to neural network hyper-parameters: Part 1--learning rate, batch size, momentum, and weight decay, arXiv preprint

arXiv:1803.09820, (2018).
[48] M.A. Soyer, N. Tüzün, Ö. Karakaş, F. Berto, An investigation of artificial neural network structure and its effects on the estimation of the low‐cycle fatigue parameters of various steels, Fatigue & Fracture of Engineering Materials & Structures, (2023).
[49] R. Elmissaoui, A. Sakly, F. M'Sahli, Optimized FPGA Implementation of an Artificial Neural Network for Function Approximation, International Journal of Emerging Trends in Engineering and Development Issue, 1(3) (2013) 2249-6149.